

Supplementary Materials

A magnetic balloon fiberbot for catheter-free angioplasty in small arteries

Han Chen^{1,2}, Yuxuan Sun^{1,2}, Han Peng^{1,2}, Yanxun Lin^{1,2}, Nian Zhang^{1,2}, Jiyu Li^{1,2}, Mengli Sui^{1,2}, Chuanxun Cai^{1,2}, Sipei Ye^{1,2}, Rui Li³, Liu Wang^{1,2,*}

¹State Key Laboratory of Nonlinear Mechanics, Department of Modern Mechanics, University of Science and Technology of China, Hefei 230026, Anhui, China.

²Institute of Humanoid Robots, School of Engineering Science, University of Science and Technology of China, Hefei 230026, Anhui, China.

³State Key Laboratory of Structural Analysis, Optimization and CAE Software for Industrial Equipment, Dalian University of Technology, Dalian 116024, Liaoning, China.

***Correspondence to:** Prof. Liu Wang, State Key Laboratory of Nonlinear Mechanics, Department of Modern Mechanics, University of Science and Technology of China, Hefei 230026, Anhui, China. E-mail: wangliu05@ustc.edu.cn

This file includes:

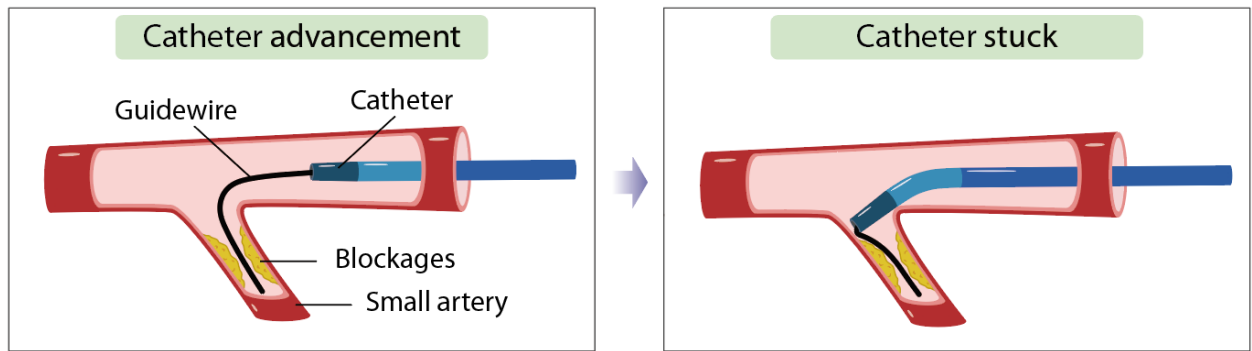
Supplementary Figures 1 to 14

Supplementary Tables 1 and 2

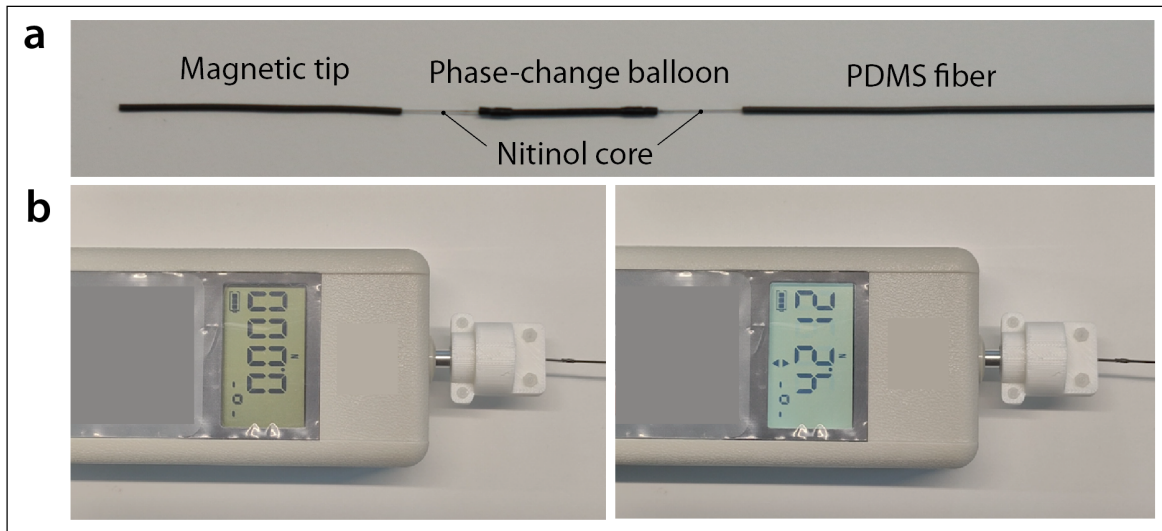
Legends for Supplementary Videos 1 to 5

Other Supplementary information for this manuscript include the following:

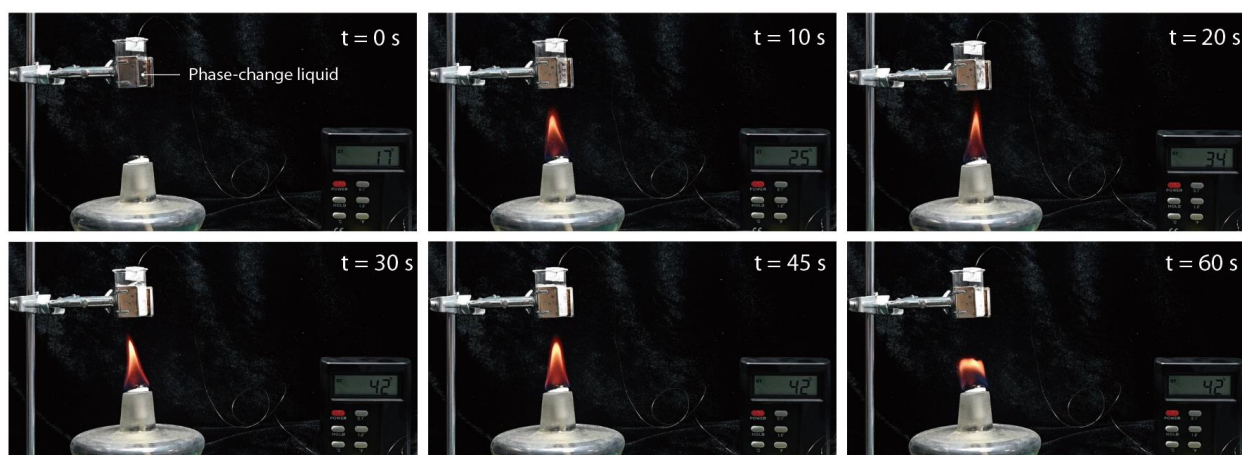
Supplementary Videos 1 to 5



Supplementary Figure 1. Schematic illustration of a catheter stuck at a tortuous small artery due to its larger size and higher bending stiffness than the guidewire.



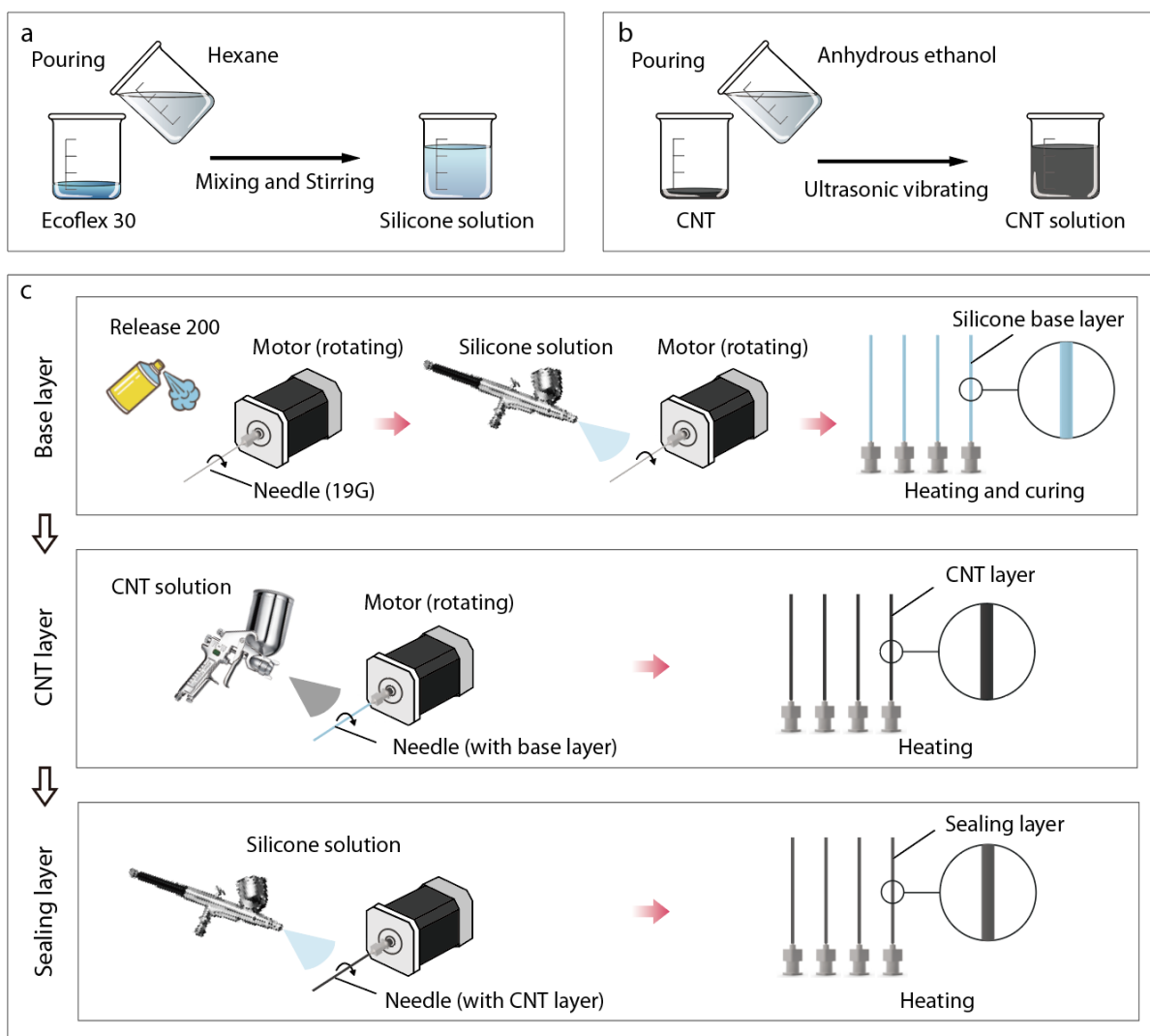
Supplementary Figure 2. Structural integration and axial tensile testing of the MBF. (a) Optical image displaying the integrated components of the MBF, where the magnetic tip, phase-change balloon, and PDMS fiber are assembled along the central nitinol core. **(b)** Axial tensile test of the MBF, demonstrating that the assembled connections can withstand a maximum tensile force of approximately 4.2 N, confirming their structural integrity (Photographed by the authors).



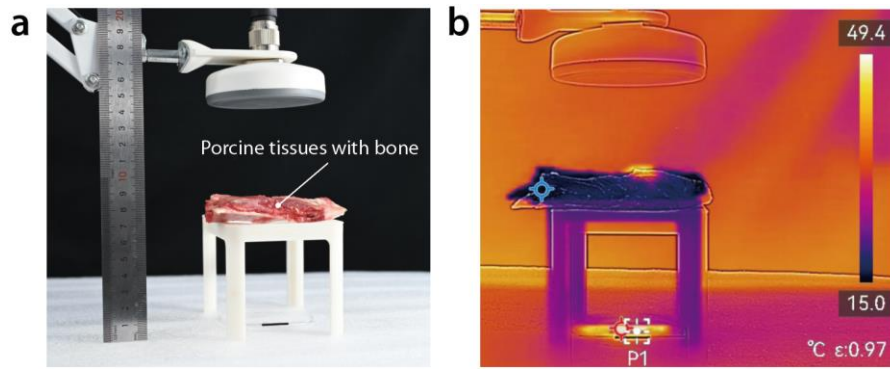
Supplementary Figure 3. Experimental verification of the intrinsic phase transition temperature (boiling point) of the Novec engineered fluid (Photographed by the authors).



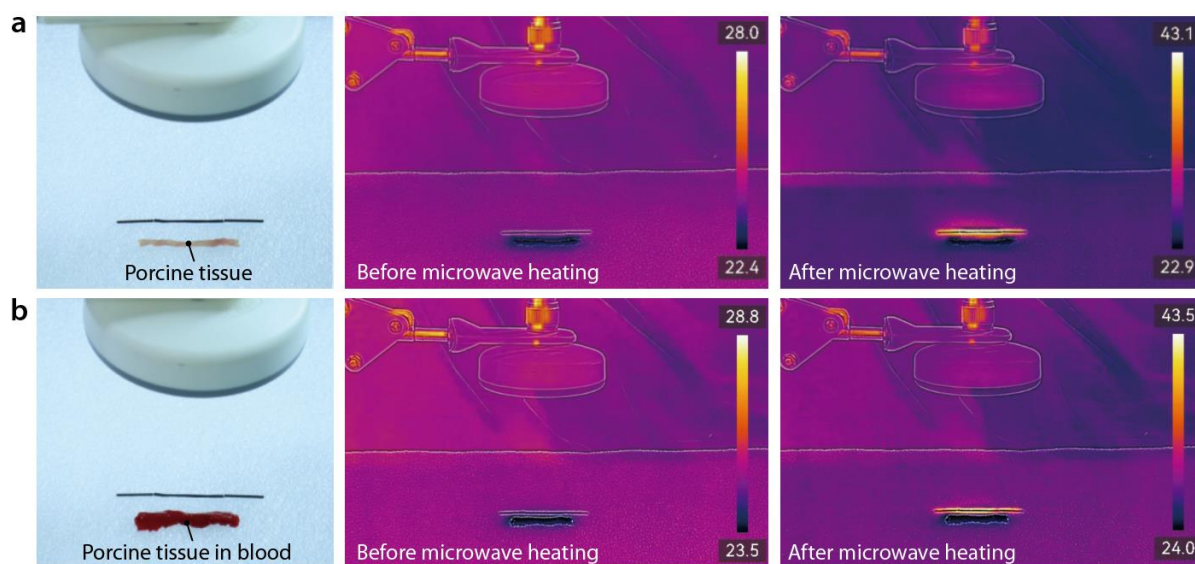
Supplementary Figure 4. Evaluation of balloon expansion behavior at different environmental temperatures. (a) At 37 °C (below the phase transition threshold), the fluid remains in a stable liquid phase and the balloon does not expand. **(b)** At 42 °C (reaching the phase transition temperature), the liquid-to-gas transition is triggered, leading to balloon expansion (Photographed by the authors).



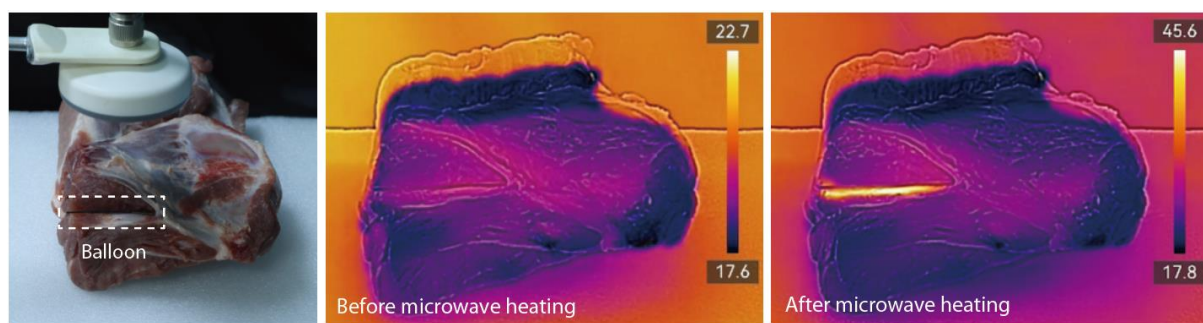
Supplementary Figure 5. Fabrication of the functionalized balloon of the MBF. **a.** Preparation of the silicone solution for spraying. **b.** Preparation of the CNT solution for spraying. **c.** The fabrication process of the Ecoflex tube begins with the spraying of the first silicone base layer on the stainless steel needle (19G), followed by the spraying of CNT on the silicone base layer, and finally the spraying of the silicone sealing layer.



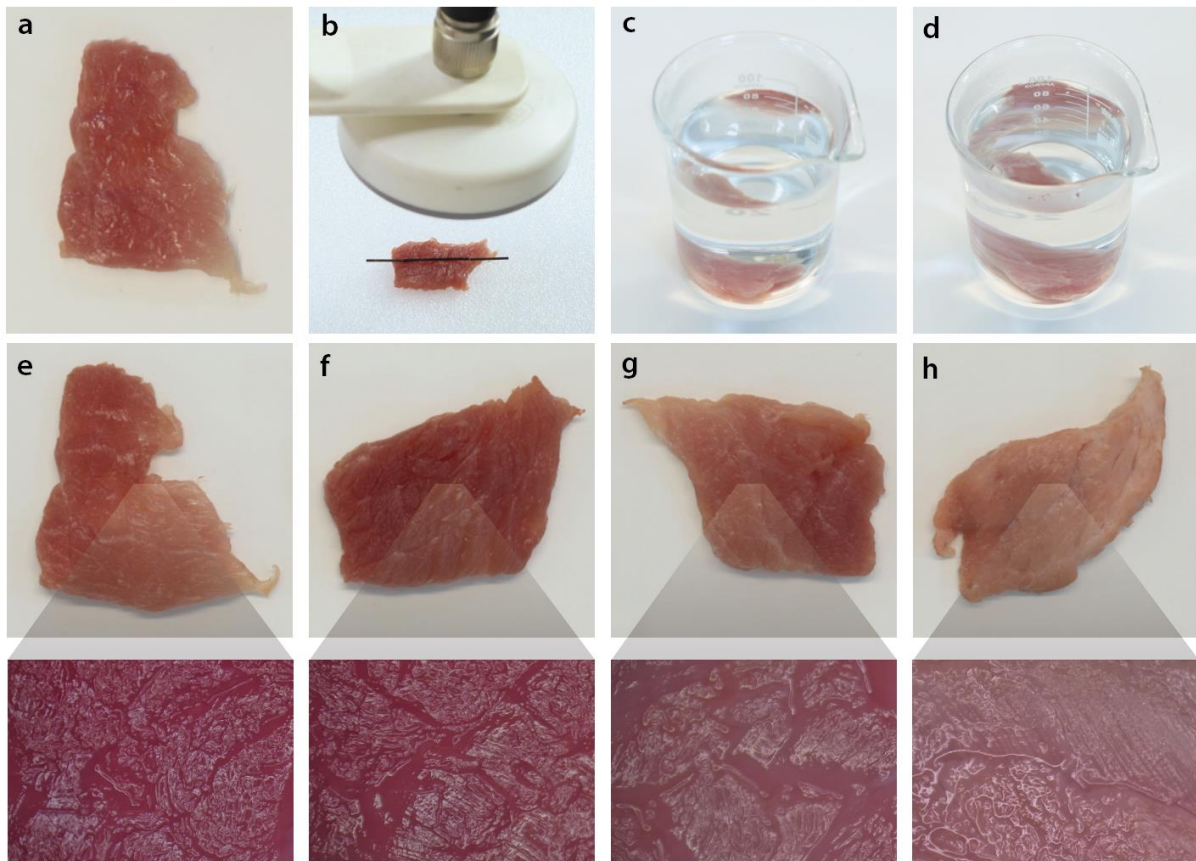
Supplementary Figure 6. Microwaves penetrate porcine tissues with bones to heat the balloon. (a) Set up of the experiment. (b) The balloon can be effectively heated above 42 °C while the porcine tissue remains nearly unheated (Photographed by the authors).



Supplementary Figure 7. Preferential microwave heating of the CNT-coated balloon under tissue-only and blood-containing conditions. (a) Comparison between the CNT-coated balloon and adjacent porcine tissue under the same microwave irradiation condition. **(b)** Comparison between the CNT-coated balloon and porcine tissue immersed in fresh anticoagulated porcine whole blood under the same microwave irradiation condition (Photographed by the authors).



Supplementary Figure 8. The thermal influence of the heated balloon on contacting porcine tissue (Photographed by the authors).

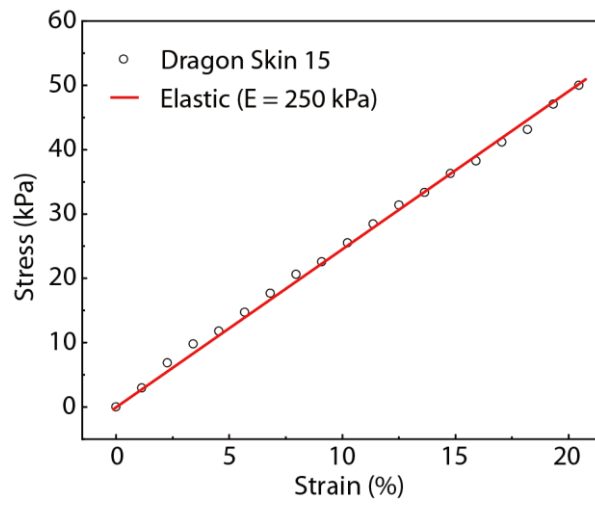


Supplementary Figure 9. Macroscopic and microscopic morphology comparison of porcine tissue after different thermal treatments.

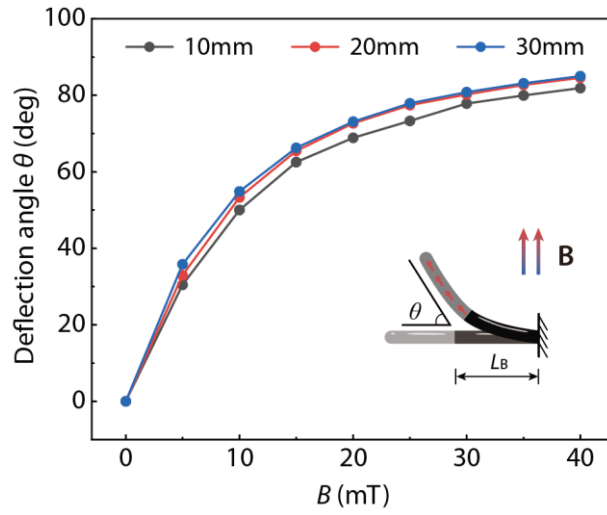
(a–d) Experimental conditions for four groups: untreated porcine muscle tissue kept at room temperature for 3 min (a); tissue contacted with the MBF during microwave heating for 3 min (b); tissue completely immersed in a 50 °C water bath for 3 min as an upper-limit whole-tissue thermal-exposure reference (c); and tissue completely immersed in a 70 °C water bath for 3 min as a high-temperature whole-tissue thermal-damage reference (d). It should be noted that the water-bath treatments in (c) and (d) represent uniform heating of the entire tissue sample, which is fundamentally different from the localized tissue contact with the microwave-heated MBF in (b).

(e–h) Macroscopic appearance of the corresponding tissue samples after treatment. The untreated control and MBF-contact microwave-heating group retained a normal reddish appearance, whereas the 50 °C water-bath group showed slight whitening and the 70 °C water-bath group showed obvious whitening.

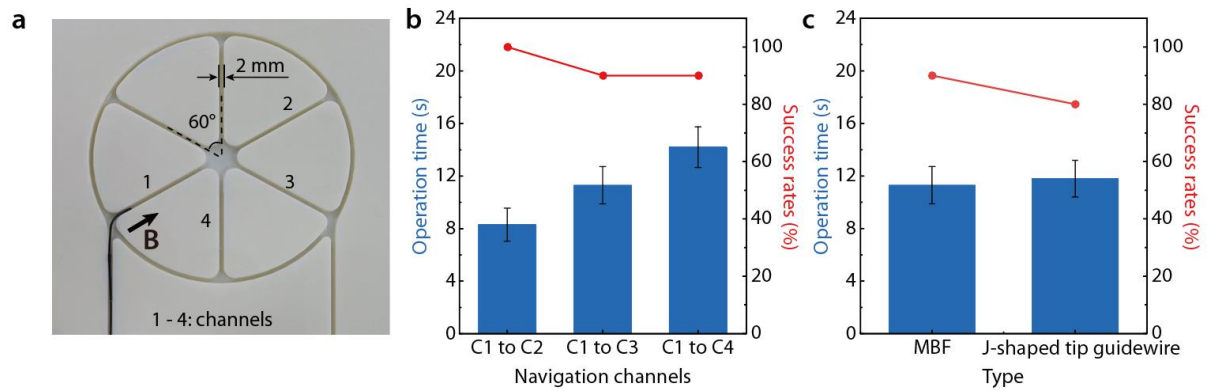
Bottom row: Microscopic surface morphology of the magnified regions indicated in (e–h). Compared with the untreated control, the MBF-contact microwave-heating group showed no obvious macroscopic or microscopic thermal alteration under the tested short-duration ex vivo condition (Photographed by the authors).



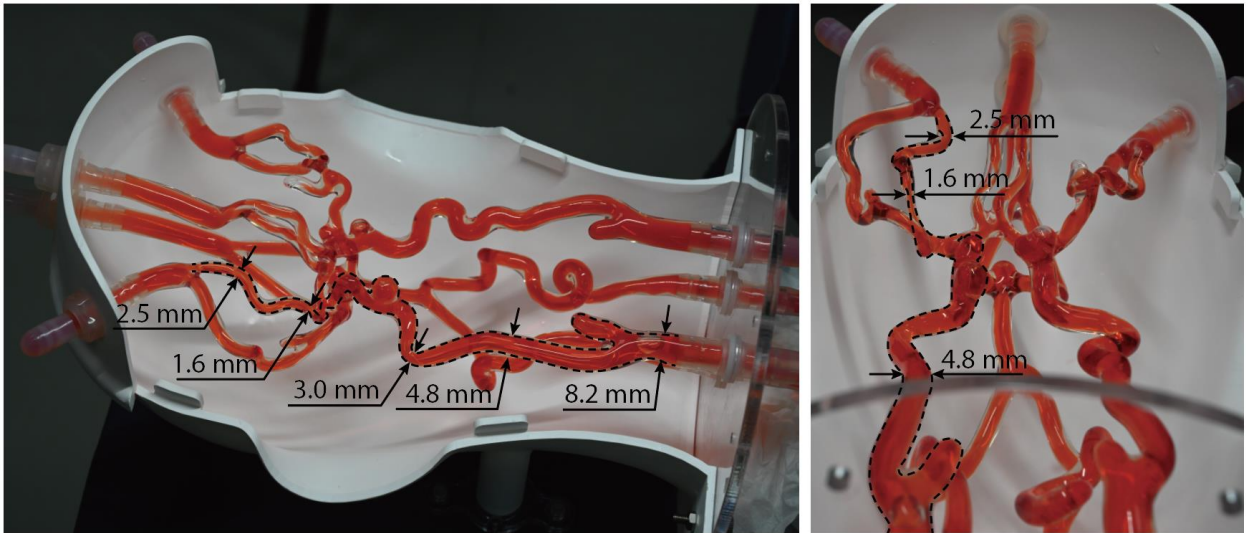
Supplementary Figure 10. Stress-strain curve of the simulated silicone blood vessel using Dragon Skin.



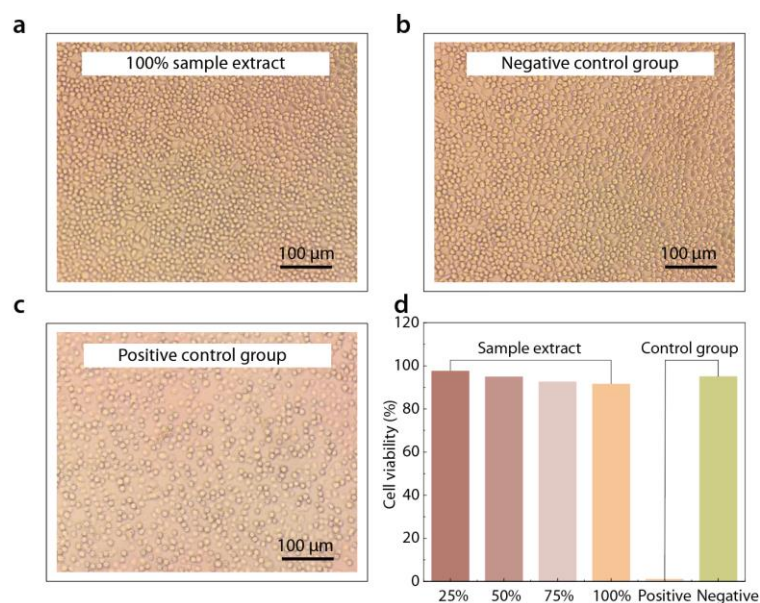
Supplementary Figure 11. Simulated deflection angle of the MBF as a function of magnetic field strength for different balloon lengths (L_B).



Supplementary Figure 12. Quantitative evaluation of navigation performance in branching channels. (a) Schematic diagram of the navigation channels. **(b)** Operation time and success rate of the MBF for navigation from C1 to C2, C1 to C3, and C1 to C4 based on 10 repeated trials. **(c)** Comparison of operation time and success rate between the MBF and a commercial J-shaped tip guidewire for navigation from C1 to C3 (Photographed by the authors).



Supplementary Figure 13. Detailed dimension of vascular pathways in the 3D cerebrovascular phantom (Photographed by the authors).



Supplementary Figure 14. The biocompatibility of MBF. L-929 cell status after 24 hours in 100% sample extract, the negative control group, and the positive control group after 48 hours at 37 °C are shown in (a), (b), and (c) respectively. The L-929 cells in both solutions exhibited no significant differences in 100% sample extract and the negative control group, indicating the MBF's good biocompatibility. The viability of L-929 cells after 24 hours of incubation in different sample extract and control groups is shown in (d). Typically, a cell viability decreases to 70% in a 100% sample extract after 24 hours suggests potential cytotoxicity. However, our 100% MBF sample extract yielded a 92% cell survival rate, significantly exceeding this threshold. This finding highlights the MBF's low cytotoxicity risk and minimal impact on cell growth and viability (Photographed by the authors).

Supplementary Table 1. Comparisons between existing approaches and our MBF for potential angioplasty application

Category	Therapeutic devices	Catheter requirement	Navigation capability	Mechanism of shape-expansion actuation	Actuation distance and power	Demonstration	Reference
Commercial guidewire/catheter	Starter™ Guidewire	Additional catheter required	Limited (Pre-shaped tip (diameter ~ 0.63 mm))	-	-	In vivo navigation	Starter™ Guidewire -Boston Scientific
Magnetic guidewires	Ferromagnetic soft continuum robot	Additional catheter required	High (Soft magnetic tip (diameter ~ 0.6 mm))	-	-	In vitro navigation	[1]
	Ultrahigh field magnetic guidewire	Additional catheter required	High (Rigid magnet tip (diameter ~ 1.0 mm))	-	-	Ex vivo navigation	[2]
	Dexterous helical magnetic robot	Additional catheter required	High (Rigid magnet tip (diameter ~ 0.7 mm))	-	-	In vivo navigation	[3]
Miniature soft robots	Miniature magnetic soft robot	Catheter-free	Limited (3 mm diameter with magnetic manipulation)	Wireless, RF heating and phase-change expansion	Inside coil (< 5 cm), ~10 kW	Ex vivo locomoting and shape-expansion	[4]
Magnetic robots	Magnetic balloon fiberbot	Catheter-free	High (Soft magnetic tip (1mm))	Wireless, microwave heating and phase-change expansion	15 cm, 50 W	Ex vivo navigation and shape-expansion	This work

Supplementary Table 2. Comparison of heating efficiency between RF heating and microwave heating

Wireless heating methods	Heating Objects	Temperature rise, ΔT (°C)	Heating power, P (W)	Heating distance, D (mm)	Heating efficiency, $\Delta T / P$ (°C/W)	Reference
RF heating	Miniature coiled artificial muscle	40	~10000	~15	0.004	[5]
	Pangolin-inspired untethered magnetic robot	80	~10000	50	0.008	[6]
	Bismuth-based metals	40	800	30	0.05	[7]
	Stiffness tunable implanted electrode	20	700	22	0.029	[8]
	Liquid-alloy hot water bag	40	345	~10	0.12	[9]
	Inchworm-like compact soft robot	30	2000	3	0.015	[10]
Microwave heating	Multi-degree-of-freedom robots	50	700	400	0.071	[11]
	MWCNTs/polypropylene composites	200	700	~140	0.29	[12]
	Rocks	80	3000	100	0.027	[13]
	Shape memory polymers	60	750	40	0.08	[14]
	Magnetic balloon fiberbot	55.8	50	150	1.12	This work

Supplementary Video 1.

In situ expansion of the MBF via low-power microwave heating (50 W at a distance of 15 cm).

Supplementary Video 2.

Accessibility tests of the MBF, a straight tip guidewire and a J-shaped tip guidewire in planar channels.

Supplementary Video 3.

Magnetic navigation of the MBF in an in vitro 3D cerebrovascular phantom.

Supplementary Video 4.

Magnetic navigation of the MBF in an ex vivo porcine placenta.

Supplementary Video 5.

Ex vivo demonstration of angioplasty in small arteries in a porcine placenta.

REFERENCES

1. Kim, Y.; Parada, G.A.; Liu, S.; Zhao, X. Ferromagnetic soft continuum robots. *Sci. Robot.* **2019**, *4*, eaax7329, doi: <https://doi.org/10.1126/scirobotics.aax7329>.
2. Tiriyaki, M.E.; Elmacioğlu, Y.G.; Sitti, M. Magnetic guidewire steering at ultrahigh magnetic fields. *Sci. Adv.* **2023**, *9*, doi: <https://doi.org/10.1126/sciadv.adg6438>.
3. Dreyfus, R.; Boehler, Q.; Lyttle, S.; Gruber, P.; Lussi, J.; Chautems, C.; Gervasoni, S.; Berberat, J.; Seibold, D.; Ochsenbein-Kölble, N.; et al. Dexterous helical magnetic robot for improved endovascular access. *Sci. Robot.* **2024**, *9*, eadh0298, doi: <https://doi.org/10.1126/scirobotics.adh0298>.
4. Tang, Y.; Li, M.; Wang, T.; Dong, X.; Hu, W.; Sitti, M. Wireless Miniature Magnetic Phase-Change Soft Actuators. *Adv Mater* **2022**, *34*, e2204185, doi: <https://doi.org/10.1002/adma.202204185>.
5. Li, M.; Tang, Y.; Soon, R.H.; Dong, B.; Hu, W.; Sitti, M. Miniature coiled artificial muscle for wireless soft medical devices. *Sci Adv* **2022**, *8*, eabm5616, doi: <https://doi.org/10.1126/sciadv.abm5616>.
6. Soon, R.H.; Yin, Z.; Dogan, M.A.; Dogan, N.O.; Tiriyaki, M.E.; Karacakol, A.C.; Aydin, A.; Esmaeili-Dokht, P.; Sitti, M. Pangolin-inspired untethered magnetic robot for on-demand biomedical heating applications. *Nat. Commun.* **2023**, *14*, doi: <https://doi.org/10.1038/s41467-023-38689-x>.
7. Duan, M.; Zhu, X.; Fan, L.; He, Y.; Yang, C.; Guo, R.; Chen, S.; Sun, X.; Liu, J. Phase-Transitional Bismuth-Based Metals enable Rapid Embolotherapy, Hyperthermia, and Biomedical Imaging. *Adv. Mater.* **2022**, *34*, 2205002, doi: <https://doi.org/10.1002/adma.202205002>.
8. Sun, X.; Guo, R.; Yuan, B.; Wang, H.; Duan, M.; Yang, Y.; Zhu, X.; Wang, X.; Chen, S.; Cheng, J.; et al. Stiffness tunable implanted electrode enabled by magnetic liquid metal for wireless hyperthermia. *Appl. Mater. Today* **2022**, *27*, 101495, doi: <https://doi.org/10.1016/j.apmt.2022.101495>.
9. Jiang, J.; Fei, W.; Pu, M.; Wu, Z. Wireless liquid-alloy-based induction heating for soft devices by alternating magnetic field: From characterization to application. *"Sens. Actuators, A"* **2022**, *340*, 113538, doi: <https://doi.org/10.1016/j.sna.2022.113538>.
10. Jung, W.; Lee, S.; Hwang, Y. Wireless Inchworm-like Compact Soft Robot by Induction Heating of Magnetic Composite. *Micromachines (Basel)* **2023**, *14*, doi: <https://doi.org/10.3390/mi14010162>.
11. Li, Y.; Wu, J.; Yang, P.; Song, L.; Wang, J.; Xing, Z.; Zhao, J. Multi-Degree-of-Freedom Robots Powered and Controlled by Microwaves. *Adv. Sci.* **2022**, *9*, 2203305, doi: <https://doi.org/10.1002/advs.202203305>.
12. Tang, L.; Wang, J.; Zhang, B.; Li, C.; Jin, H. Remarkable microwave heating performance of MWCNTs/polypropylene composites verified by electromagnetic-thermal coupling experiment and simulation. *Compos. Sci. Technol.* **2022**, *223*, 109428, doi: <https://doi.org/10.1016/j.compscitech.2022.109428>.
13. Hassani, F.; Nekoovaght, P.M.; Gharib, N. The influence of microwave irradiation on rocks for microwave-assisted underground excavation. *J. Rock Mech. Geotech. Eng.* **2016**, *8*, 1-15, doi: <https://doi.org/10.1016/j.jrmge.2015.10.004>.
14. Wang, Y.-C.; Wang, Y.-Z.; Shu, J.-C.; Cao, W.-Q.; Li, C.-S.; Cao, M.-S. Graphene Implanted Shape Memory Polymers with Dielectric Gene Dominated Highly Efficient Microwave Drive. *Adv. Funct. Mater.* **2023**, *33*, 2303560, doi: <https://doi.org/10.1002/adfm.202303560>.